Wireless bioelectronic device for wound healing

Prabhat Baniya[a,*], Maryam Tebyani[a], Wan Shen Hee[a], Houpu Li[a], Narges Asefifeyzabadi[a], Hsin-ya Yang[b], Kan Zhu[b,c], Gordon Keller[a], Celeste Franco[a], Kaelan Schorger[a], Koushik Devarajan[a], Alexie Barbee[a], Cristian Hernandez[a], Tiffany Nguyen[a], Fan Lu[d], Anthony Gallegos[b], Cynthia Recendez[b,c], Roslyn Rivkah Isseroff[b], Min Zhao[b,c], Marcella Gomez[d], Marco Rolandi[a,*], Mircea Teodorescu[a,e,*]

[a]*Department of Electrical and Computer Engineering, University of California Santa Cruz, Santa Cruz, 95064, California, USA*
[b]*Department of Dermatology, School of Medicine, University of California Davis, Sacramento, 95816, California, USA*
[c]*Department of Ophthalmology & Vision Science, University of California Davis, Sacramento, 95817, California, USA*
[d]*Department of Applied Mathematics, University of California Santa Cruz, Santa Cruz, 95064, California, USA*
[e]*Genomics Institute, University of California Santa Cruz, Santa Cruz, 95064, California, USA*

Abstract

Wound healing is a prolonged biological process that goes through multiple phases spanning several weeks. In order to improve wound healing, we introduce a wireless, bioelectronic device that can deliver various treatments for multiple days while continuously monitoring the delivery. Devices are developed for delivery of fluoxetine cations (Flx^+) and electric field (EF) in freely moving pigs. The treatments can be controlled and monitored real-time via WiFi, with options for both user specified delivery rate and duration as well as automated closed-loop control. The devices are designed to handle various failure scenarios that can come in dynamic, real-world experiments such as communication and power interruptions so that valuable experimental data can continue to be gathered. The ion pump on the wireless device consists of eight channels, arranged in a circular pattern near the edge of a 20 mm diameter wound, to deliver charged biomolecules such as Flx^+. For EF delivery, an additional center reference channel is provided. When the applied voltages at the outer eight channels are higher than the center channel, it results in the applied EF to be in the same direction as the endogenous EF and aids the healing process. The device locally records the applied voltages and currents as a function of time on a microSD card at a high sampling rate while simultaneously sending real-time measurements, via a local WiFi network to a wound healing algorithm, running on a remote laptop. The closed-loop control of current/delivery rate is done by onboard microcontroller unit (MCU) and current sources based on the instructions received from the wound healing algorithm. A graphical user interface (GUI) is developed to provide seamless user control and data viewing capabilities with support for multiple devices. Using immunohistochemistry (IHC) staining, we found that the M1/M2 ratio of a Flx^+—treated wound at the edge had improved by 70.2% compared with a control wound, both harvested after three days of wound creation. Similarly, using hematoxylin and eosin (H&E) staining, we found that the re-epithelialization of a Flx^+-treated wound had improved by 39.5% compared with a standard-of-care wound, both harvested after seven days of wound creation. Both of these results indicate the potential of the wireless bioelectronic device to improve wound healing.

Keywords: Wireless, Bioelectronics, Drug delivery, Wound healing

1. Introduction

Wearable and implantable bioelectronic devices have applications in remote health monitoring (Cascales et al., 2020), wound healing (Freedman et al., 2023), diabetes, cancer, contraception, and treatment of various other diseases (Kar et al., 2022). Wound healing treatment presents one of the major medical challenge to date. Advancements in wound care include various types of smart dressings and patches for promoting wound healing (Mirani et al., 2017; Chi et al., 2020; Mostafalu et al., 2017) through thermo-responsive mechanism of drug and antibiotic delivery, necessitating the need for micro heater and external power supply (Xu et al., 2021). Other traditional devices rely on wiring to bulky power supplies for applying exogenous electric field with manual tuning of the field strength to accelerate wound closure (Chen et al., 2021; Liang et al., 2020) with limited practicality for achieving real-time treatment. Self-powered and self-activated wearable piezoelectric (Du et al., 2020) and triboelectric nano-generators for electrical stimulation (Long et al., 2018) and drug delivery (Ouyang et al., 2019) have been demonstrated but are limited to skin wound healing with little control over stimulation strength or release profile. Electronic drug delivery (EDD) systems exists that allow more precise spatio-temporal control of drug release rate, timing, and dosage while reducing systemic side effects and improving patient compliance (Liu et al., 2023, 2022; Vadlapatla et al., 2017) in wound healing applications (Li et al., 2023a). In EDD systems, the rate and total dose of charged drug molecules are controlled by monitoring and changing the stimulation current am-

*Corresponding authors.
Email addresses: pbaniya@ucsc.edu (Prabhat Baniya), mrolandi@ucsc.edu (Marco Rolandi), mteodore@ucsc.edu (Mircea Teodorescu)

plitude and duration, respectively, that allows for better drug penetration and sustained delivery into the tissue than traditional oral and needle-based (hypodermic) delivery (Song et al., 2014; Mori et al., 2023; Bakshi et al., 2020). Moreover, wireless EDD devices can provide ease of connectivity (Ghanim et al., 2023) for real-time, continuous monitoring and remote control of drug dose to provide local on-demand drug delivery (Liu et al., 2020; Mostafalu et al., 2018; Vadlapatla et al., 2017; Del Bono et al., 2023; Li et al., 2023b). Furthermore, wireless devices enable experimentation on multiple freely-moving animals (each animal could additionally carry multiple devices) providing more data and larger sample size in each experiment and animal behavior is minimally altered compared to a tethered system (Wentz et al., 2011), enabling better statistical analysis. Due to limited space at the wound site, small yet efficient antenna designs are important for realizing reliable wireless links for bidirectional communication, in spite of variable antenna orientation, interference between multiple devices, and detuning in the presence of bodily tissues, particularly for ingestible bioelectronics (Khan et al., 2022). Notably, wearable wireless devices have also been demonstrated in vivo for accelerating wound healing. Most recently, a wireless bioelectronic system was demonstrated for antibiotic drug delivery (TCP-25 AMP) in combination with electrical stimulation for treating infected chronic wounds in mouse models while monitoring wound infection and inflammatory bio-markers such as temperature, pH, ammonium, glucose, lactate, and uric acid (Sani et al., 2023). A wirelessly controlled micropump in combination with microneedle array has been used for controlled release of VEGF with specific temporal profiles in diabetic mice (Derakhshandeh et al., 2020). This system achieves improved wound closure by utilizing microneedle arrays to transdermally reach deeper layers of the wound bed and improve the bioavailability and effectiveness of drugs delivered. Electronically controlled antibacterial cefazolin delivery through close-loop feedback obtained via sensing of temperature, pH, and uric acid of wound has also been shown to treat infection and increase wound closure rates in rats, as demonstrated by (Xu et al., 2021). Use of electrically stimulated hydrogel electrodes was demonstrated by (Jiang et al., 2022) to reduce wound size and increase dermal thickness in mice through close-loop control of the stimulation in response to changes in wound impedance and temperature.

However, there have been limited reports of prolonged actuation in vivo experiments spanning 7 days or more that continuously monitors dose delivery during the wound healing process. We propose a fully integrated wireless bioelectronic device comprised of polydimethylsiloxane (PDMS) reservoirs that holds charged drug molecules in solution and a printed circuit board (PCB) that applies voltages to drive small electrical currents through the solution and push the drug molecules through hydrogel-filled capillaries and into the wound. The wireless device is validated and verified through in vitro, ex vivo, and in vivo experiments. The electrical currents are monitored in real-time and wirelessly on a graphical user interface (GUI) running on a nearby laptop. The users are also able to remotely control the devices in real-time to start, stop, or change the actuation if/when needed. The devices can also be placed in closed-loop mode with a laptop to control the drug delivery rate based on predefined target current levels. Table 1 compares our work with other similar works reported in the literature.

2. Materials and methods

2.1. Ethics statement

All animal experiments were conducted under the protocol approved by the University of California Davis (UC Davis) Institutional Animal Care and Use Committee (IACUC). All methods were performed in accordance with the UC Davis IACUC guidelines and regulations. All animal studies are reported in accordance with ARRIVE guidelines.

2.2. PCB fabrication, assembly, and modeling

The PCBs are designed in Autodesk EAGLE, as shown in Fig. 1a. The prototypes are fabricated and assembled by a third-party PCB manufacturer. The contact pins are hand soldered to the plated through holes (PTHs) on the PCB. The 3D models of the PCBs are created in Autodesk Fusion 360 (Baniya et al., 2023; Pansodtee et al., 2021).

2.3. 3D printing of PDMS molds

The CAD models of the PDMS molds are created in Autodesk Fusion 360. The STL files of the models are imported into the Formlabs PreForm software. The models are optimized for print orientation, layout, and supports before uploading the resulting file to the Formlabs Form 3 SLA printer for printing with Model V2 resin (Baniya et al., 2023).

2.4. Hydrogel-filled capillary preparation

In order to deliver ions such as Flx^+, silica capillaries are filled with a polyanion hydrogel that selectively conducts cations, following the process detailed in (Baniya et al., 2023; Dechiraju et al., 2022; Asefifeyzabadi et al., 2024). The hydrogel recipe requires 1 M AMPSA, 0.4 M PEGDA, and 0.05 M photoinitiator (I2959) concentrations to result in a hydrogel with a low swelling ratio (12%) and good conductivity (8.8±0.1 S/m). A several-centimeter length of the silica tubing (inner diameter 0.8 mm, outer diameter 1 mm) used for the capillaries is etched with NaOH and further treated with silane A174 to prevent the hydrogel from swelling out of the capillary after UV crosslinking for 5 min at 8 mW/cm^2. Following UV curing, the capillary tubes are cut into 5 mm pieces. This designated length allows for the easy insertion of capillaries into the PDMS device, with minimal cutting required to get the capillaries down to the required 3 - 4 mm final length. Cutting the capillary tubing into small lengths beforehand also allows each tube to be checked for electrical connection and loaded with Flx^+. The capillaries are first soaked in a 0.1 M HCl solution for several hours. Both ends of the capillary are then placed in electrolyte wells made from PDMS on a glass slide. 0.5 mm diameter Ag and AgCl wires are used as the working electrode (WE) and reference electrode (RE), respectively, and are inserted at the two ends of each capillary to be loaded. The wells are filled

Device	Drug delivered	Animal model	Actuation parameters	Wound healing mechanism
Wireless bioelectronic system (this work)	Fluoxetine & ES	Pig	3.3 V, 2 - 20 μA, 6-12 h DC/Pulsed DC	Reepithelialization M1/M2
Wireless, stretchable bioelectronic system (Sani et al., 2023)	TCP-25 AMP & ES	Mice	1 V, 1 mA, 10-20 min DC	Antibacterial
Wireless micropump/microneedle system (Derakhshandeh et al., 2020)	VEGF	Diabetic mice	3 V, 10 min	Vascularization
Wireless smart wound dressing (Xu et al., 2021)	Cefazolin	Rat	-0.5 V, 90 s DC	Antibacterial
Wireless, closed-loop, smart bandage (Jiang et al., 2022)	ES	Mice	0-2 V, 6 h, 13.56 MHz rectified AC	Proregenerative macrophage

Table 1: Wireless bioelectronic system in comparison with other wearable, wireless bioelectronic systems used for wound healing in animal models.

with 0.01 M Flx-HCl (source solution) at the WE end and 0.01 M KCl (target solution) at the RE/counter electrode (CE) end. To avoid water splitting, +0.8 V is applied at the WE for 5 min. A clean steady-state current is obtained when there are no hydrogel issues. The typical steady-state current measured when loading the capillaries with Flx^+ is 2 μA. Each device has 9 hydrogel-filled capillaries inserted in them.

2.5. Animal experiments

Yorkshire-Landrace-Duroc mixed breed pigs, female, 70-80 lbs, about 4-5 months old, were used. As shown in Fig. 1b, 8 circular, 20 mm diameter full-thickness (which reaches the muscle layer), excisional wounds are created, 4 bilaterally on each side of the dorsum on each animal. The actuation device was applied to the first 4 wounds (treatment group: wounds 1, 2, 5, 6) nearest to the head while 4 wounds nearest to the tail were controls: 2 device controls (no actuation, wounds 3 and 7) and 2 biological controls (no device, wounds 4 and 8). Wounding surgery day is designated to be Day 0. The pigs were acclimated 10 days prior to the surgery with daily behavioral training and harness use. The animal identification and the initial weights were recorded. The pigs were singly housed and behavioral trained daily with positive reinforcement/food treats (fresh fruit and yogurt loaded in feeding bottles) to stand still for future post-op check. Briefly, the animals were fasted for 12 hours prior to the surgery. The pigs were induced under general anesthesia, intubated endotracheally and maintained under anesthesia using masked inhalation of Isoflurane (1-5%) to effect in 100% oxygen. Vital signs (heart rate, respiratory rate and temperature) were monitored every 15 min. A blood sample was collected in the beginning of the surgery. The surgery area was clipped, depilated and prepared with 2% chlorhexidine scrubs and isopropyl alcohol rinses and a final betadine spray. After that, the 8 circular wounds were surgically created. Wound images were taken by a camera (connected externally to Raspberry Pi) mounted on top of each wound. As illustrated in Fig. 1b, for the 2 biological control wounds 4 and 8 (nearest to the tail end), regular wound dressings (Conformant 2 wound veil, Optifoam bolsters, and Tegaderm film dressings) were applied.

Six devices with 2 sets of Raspberry Pi (for imaging) and power bank were applied to the 4 actuated wounds and 2 device control wounds. Each Raspberry Pi captures camera images from 3 devices. At the end of the surgery, the entire wound area was covered with cushion foam sheets and a compression dressing/pig jacket to protect the wounded area. Analgesic medication buprenorphine was given at extubation and a fentanyl patch was applied for 72 hours for the post-op pain management.

For the treatment group, the devices and wounds were examined every morning during the post-op period. Daily Flx was delivered from the actuator device for 6 hours for 7 days and the camera that sits above the wound, as shown in Fig. 1b, captured the wound images every 2 hours. The daily actuation cycle started after the replacement of power banks while the animal stood still with treats (no additional anesthesia required). At the endpoint, the animals were anesthetized briefly to collect blood samples, and then euthanized with pentobarbital > 100 mg/kg IV. The devices were retrieved, the wounds were imaged again by the camera, and swabbed with sterile cotton tips for bacterial counts. Then the wound tissue was harvested and bisected to preserve in PBS for fresh tissue, or be fixed in 4% paraformaldehyde, or RNALater for histological analysis and gene expression profiles.

2.6. Histology

At the end of each experiment, after euthanizing the pigs, whole wounds were excised and bisected, and one half of the wound was placed into a paraformaldehyde solution to fix for 96 h, to ensure adequate fixation and infiltration prior to embedding. One half of the tissue was used for dissociation and FACS analysis to optimize this protocol. The PFA-fixed tissues were processed in a tissue processor for FFPE tissue histology, and the processed tissues were embedded into paraffin blocks and cut into 5 μm thick sections using a microtome. The sections were placed onto glass slides and, after some drying time, the sections were stained using hematoxylin and eosin (H&E) protocol to determine re-epithelialization. The following protocol was utilized:

1. Deparaffinization Slides were placed in 2 washes of Xylenes for 5 minutes each, followed by neat ethanol (10

dips), neat ethanol (10 dips), 95% ethanol (10 dips), 70% ethanol (10 dips), and water (10 dips). Pre-warm Sodium Citrate pH 6.0 in the rice cooker after the Xylene washes.

2. Hematoxylin staining Slides were placed in hematoxylin for 11 minutes, rinsed water (10 dips), differentiated in 5% HCl in 70% ethanol (1 dip), rinsed with water (10 dips), and blued in lithium carbonate solution (5 dips), and rinsed twice with water (10 dips each).
3. Hematoxylin staining Slides were placed in hematoxylin for 11 minutes, rinsed water (10 dips), differentiated in 5% HCl in 70% ethanol (1 dip), rinsed with water (10 dips), and blued in lithium carbonate solution (5 dips), and rinsed twice with water (10 dips each).
4. Coverslipping Immediately after eosin staining and differentiation, slides were rinsed with 95% ethanol (10 dips), 95% ethanol (10 dips), neat ethanol (10 dips), neat ethanol (10 dips), neat ethanol (10 dips), xylenes (10 dips), xylenes (10 dips), and the slides were held in a final rinse of xylenes during coverslipping. A small drop of Cytoseal 60 was placed onto the tissue sections and a glass coverslip was carefully mounted to avoid trapping air bubbles underneath.

The stained sections were imaged using a Keyence BZ-9000 inverted microscope in the brightfield channel.

2.7. *Macrophage IHC staining*

To analyze the phenotypic alterations in macrophages during pig wound healing following Flx and/or EF delivery, we developed a robust immunohistochemistry (IHC) protocol featuring quadruple staining to unveil M1/M2 profiles within the same tissue section. This assay encompasses the preparation of experimental pig tissues, involving their embedding in paraffin, followed by sectioning and subsequent staining. This staining process entails the application of specialized antibodies tailored to discern distinct macrophage markers. Within each wound sample, four distinct fluorescent markers are employed, providing the foundation for establishing a comprehensive macrophage panel. These markers encompass: 1) DAPI: Labels all cell nuclei. 2) CD68 (BA4D5): Marks pan-macrophage cells. 3) iNOS: Identifies M1-like macrophages. 4) Arginase I: Identifies M2-like macrophages. Identification of M1 and M2 cells is based on the combination of fluorescent signals. An M1 cell is distinguished by fluorescence in DAPI (blue), CD68 (green), and iNOS (yellow), whereas an M2 cell exhibits fluorescence in DAPI (blue), CD68 (green), and Arginase I (red). This quadruple-staining technique ensures a precise representation for subsequent M1/M2 ratio calculations. To accomplish this, a customized Cell Profiler pipeline is employed for the recognition of double-positive cells. These cells are subsequently semi-quantified to ascertain the M1/M2 ratio. This calculation proves pivotal in comparing treated and control wounds, offering vital insights into the efficacy of bio-engineered PDMS devices in delivering Flx and/or EF. This assay plays a critical role in comprehending the influence of these treatments on macrophage polarization and, consequently, wound healing.

The IHC protocol is completed over two days. Wound tissue is harvested, fixed in paraformaldehyde, embedded in paraffin and sectioned by the Isseroff team, and paraffin embedded slides delivered to our team for IHC analysis. First the slides are warmed for 30 - 60 min at 60° C, followed by deparaffinization of the slides with 3 xylene washes on a shaker totaling one hour, then followed by 5-min washes in a graded alcohol station, starting from 100% ethanol going to 50% ethanol, and then finally ending with PBS washes. Slides then undergo the antigen retrieval step in a rice cooker/vegetable steamer for 40 min, in a bath of EDTA Ph 8.0. Slides are cooled for 30 min. PBS/PBST washes are performed for 1 h total. Slides are then blocked with 10% Donkey Serum + 3% BSA + PBST (tritonx-100 at 1%) for 2 hours at room temperature in a humidified slide box. Primary antibodies are then incubated overnight at room temperature for 12-16 h in a humidified slide box. Primary antibodies are incubated at the following dilutions: iNOS 1:50 (Thermo fisher, cat # PA1036), Arginase I 1:50 (Thermo fisher, cat # PA518392), and BA4D5 1:20 (Bio-Rad, cat # MCA2317GA). Next day, slides are washed for 1 hour in PBS and PBST. Then incubated for 1.5 h in 1:200 diluted secondary antibodies dyed with different Alexafluors. Afterward, a TRUEVIEW autofluorescence kit is added for 5 min, followed by a 15-minute incubation in DAPI. Then slides are mounted with nail polish and imaged on Zeiss Confocal LSM 900. After imaging, photos are viewed through ImageJ and analyzed using a program called Cell Profiler to label colocalization and help manual counting of each image. Eight images are taken, 4 in the wound center and 2 on both wound edges.

2.8. *PDMS ion pump*

The PDMS ion pump is inserted into the wound for Flx or EF delivery, as shown in Fig. 1b. The design and fabrication of the PDMS ion pump follows a process similar to the one outlined in (Baniya et al., 2023; Asefifeyzabadi et al., 2024; Dechiraju et al., 2022). Fig. 1a shows how the PDMS ion pump CAD model which is fabricated from 3D printed two-part molds. The printed molds are filled with PDMS and then cured. The top and bottom PDMS pieces are then demolded and bonded together. The top PDMS contains the reservoirs to store drug solution of interest and through-holes for electronics interfacing. The bottom PDMS functions as a lid to seal the reservoirs and contains a notch which has a diameter of 20 mm and depth of 8-10 mm that roughly matches the wound dimensions. The notch has 9 vertical channels (8 at the edge, 1 at the center) that connect the reservoirs to the wound bed. Hydrogel-filled capillaries are inserted at the bottom of the channels to prevent solution leakage while passing positively charged ions/biomolecules to the wound when voltage is applied. A deep cut is performed at the wounding site to remove the thick fat layer so that the notch can be inserted to reach the muscle layer, as shown in Fig. 1c. A clamp is used to seal the reservoirs between the two pieces to ensure good manufacturing yield. The bottom PDMS base thickness (optical path) is chosen so that the camera has a good focus of the wound bed through its lens, as shown in Fig. 1b and d. A larger capillary tubing is utilized to increase the ion pump current and delivery output. As illustrated

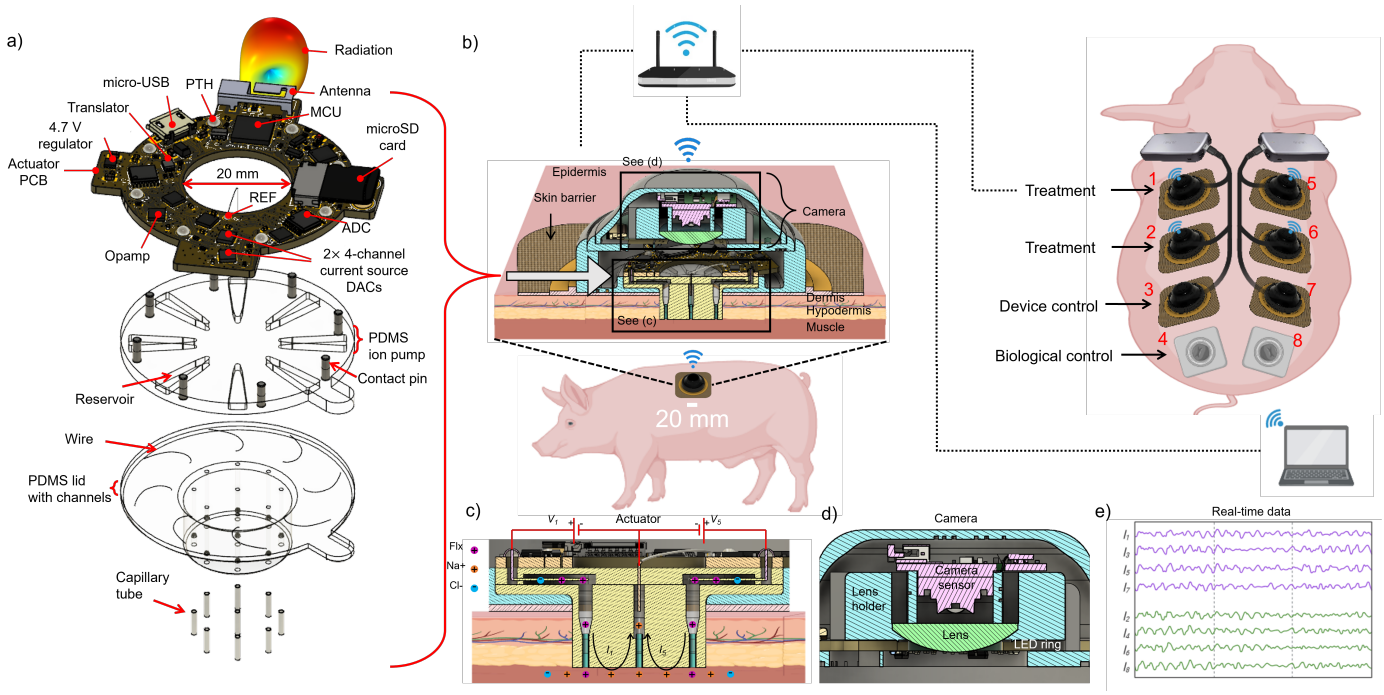

Fig. 1. a) Exploded view of integrated PCB-PDMS porcine device. b) Wireless bioelectronic devices are placed on the back of the pigs for wireless communication with remote laptop for real-time data acquisition and control of drug (Flx^+) and EF delivery. c) Cross-sectional view of the actuator. d) Cross-sectional view of the camera (sensor). e) Illustration of real-time data acquisition of current.

in Fig. 1c and detailed in (Baniya et al., 2023), the ion pump operates by applying a positive voltage V_i between a WE at a reservoir and RE at the center, which pushes drug cations (e.g., Flx^+) through cation-selective hydrogel-filled capillaries from the reservoir into the wound bed in exchange for endogenous sodium cations (Na^+) at the RE. Fig. 1e illustrates the real-time data acquisition of channel currents.

3. Results and Discussion

3.1. Experimental setup

Fig. 1b shows the experimental setup on pig for 7-day Flx delivery. The devices are placed on the backs of the pigs and communicate wirelessly to a remote laptop through a local WiFi network that is set up using a commercial router. Eight wounds (left: 1, 2, 3, 4; right: 5, 6, 7, 8) were created on each pig. Wound 1, 2, 5, and 6 are used as treatment group, wounds 3 and 7 are used as device control group, and wounds 4 and 8 are used as standard-of-care group (no devices). The actuated devices wirelessly receive commands and send measured voltages and currents to a remote laptop.

3.2. Design of wireless bioelectronic PCB

Fig. 1a shows the CAD model of the wireless bioelectronic PCB with WiFi/Bluetooth capable microcontroller unit (MCU), microSD card, analog-to-digital converters (ADCs), and current-source digital-to-analog converters (DACs) with the ion-pump PDMS underneath. As shown in Fig. 1a, the PCB ring has a 43 mm outer diameter with a 20 mm inner diameter. There are 8 plated through holes (PTHs) of 1.75 mm diameter each, where contact pins or electrode wires can be inserted to achieve mechanical and electrical integration with the PDMS ion pump piece underneath. The holes are located at a radial distance of 19 mm from the center. The simplified circuit diagram of the PCB is shown in Fig. 2a. The I^2C clock and data pins of the onboard MCU (Espressif ESP32-PICO-D4) are connected to the respective pins of the DAC and ADC to carry out instructions for setting the applied voltages at the electrodes (actuation) and reading the differential voltages at the current sensing resistors (sensing), respectively. The PCB ring has a micro-USB connector for powering the electronics. The connector is also utilized to flash the onboard MCU chip with the control program, using a USB-A/C port of a laptop. As shown in Fig. 2a, the DAC outputs are connected to the contact pins in PDMS and the ADC measures the current I_i through each channel i by finding the voltage drop across a high-precision (0.1%), current-sense resistor $R_i = 10\,k\Omega$. As shown in Fig. 2a, each PDMS reservoir/vertical channel i can be modeled as an equivalent circuit consisting of a parallel combination of equivalent capacitance C_{eq_i} and resistance R_{eq_i} in series with channel resistance R_{ch_i}. The channel resistance R_{ch_i} is a function of contact resistance, solution resistance, hydrogel-filled capillary resistance, and device geometry (shape and size of the reservoirs and channels). R_{eq_i} is a function of charge-transfer resistance R_{ct_i} at the electrode-electrolyte interface. C_{eq_i} is a function of double-layer capacitance C_{dl_i} at the electrode-electrolyte interface, capillary capacitance C_{p_i}, and wound capacitance C_w. The biological sample under actuation represents the wound resistance R_w which is mostly resistive in nature for deep tissue layer such as muscle.

Fig. 1a shows the steps involved in the integration of the PCB with the PDMS. The top and bottom view of the fabricated prototype of the PCB is shown in Fig. 2b and c. The PCB has 8 plated through-holes (PTHs) for electrical/mechanical integration with PDMS. The integration is achieved with the help of 8 Pt-coated pins that are inserted into the PDMS through-holes, as depicted in Fig. 1a. Each pin has a diameter and length of 1.6 mm and 4.8 mm, respectively. The pins are made of low-alloy steel but are Pt-coated to prevent corrosion. Conductive silver epoxy paste are manually coated on the bottom half before the pins are inserted into the PDMS through-holes. Therefore, each pin is electrically connected with the embedded electrodes in the PDMS holes. The 8 PTHs of the PCB mechanically align with the PDMS through-holes, allowing the PCB to be placed flush on the PDMS by guiding the PTHs over the pins. The protruding top portion of the pins is soldered to the pads of the PTHs to complete the PCB-PDMS integration, as shown in Fig. 1a. Next, using a syringe, each reservoir is filled with either a protonated Flx HCl solution or Steinberg solution, depending on whether Flx or EF is to be delivered, as shown in Fig. 1a. After that, as depicted in Fig. 1a, hydrogel-filled capillaries are manually inserted (using a push metal) in the 9 channel outlets at the bottom of the PDMS. The capillaries provide cation-selective electrical path between the reservoirs' solution and the biological sample that is in contact with the device. Finally, the entire device is enclosed in a 3D-printed case, as shown in Fig. 1b, to provide protection against physical forces caused by animal movement.

For the equivalent circuit model in Fig. 2a, the current I_i at each channel i for an applied voltage V_i is the sum of capacitive I_{c_i} and resistive I_{r_i} terms and is given by

$$I_i(t) = I_{c_i}(t) + I_{r_i}(t) \tag{1}$$

The capacitive term can be modeled as

$$I_{c_i}(t) = \frac{V_i}{(R_{ch_i} + R_w)} e^{-\frac{(R_{eq_i}+R_{ch_i}+R_w)t}{R_{eq_i}(R_{ch_i}+R_w)C_{eq_i}}} \tag{2}$$

where the initial charging path of the current only includes R_{ch_i} and R_w since C_{eq_i} initially acts as a short-circuit due to its zero charge.

The resistive term can be modeled as

$$I_{r_i}(t) = \frac{V_i}{(R_{eq_i} + R_{ch_i} + R_w)} \left(1 - e^{-\frac{(R_{eq_i}+R_{ch_i}+R_w)t}{R_{eq_i}(R_{ch_i}+R_w)C_{eq_i}}}\right) \tag{3}$$

where the steady-state (resistive) path of the current includes R_{ct_i}, R_{ch_i}, and R_w since C_{eq_i} acts as an open-circuit once it is fully charged.

The detailed circuit diagram in Fig. 3 shows the circuitry for microUSB-to-serial converter for flashing, voltage regulation and filtering, impedance matching for antenna, 16-channel analog-to-digital converter (ADC), 8-channel digital-to-analog converter (DAC), current sensing resistors, microSD serial peripheral interface (SPI) interface for data storage, and operational amplifiers as buffers. An LED is also included that connects to a MCU GPIO pin to indicate the WiFi connection status. It blinks when the MCU is attempting to connect to a WiFi network and turns OFF once the connection is established. An unregulated 5 V output from a power source (e.g., a power bank or battery) is regulated down to 3.3 V as the supply voltage for the MCU, and to 4.7 V as the supply voltage for the DACs, and ADCs, using two separate low-dropout (LDO) regulators, as shown in Fig. 3. Moreover, a schottky diode is placed in series between the 5 V rail and the 3.3 V LDO input to provide reverse current protection for the MCU and USB port.

3.2.1. DAC, ADC, and Translator

As shown in Fig. 2a, the actuation and sensing circuitry consists of DAC and ADC respectively. Both utilize a higher supply voltage of 4.7 V. Given that the 5 V output from most power sources is unregulated, it cannot be directly used to power the circuitry, limiting the measurement accuracy. Therefore, a low-dropout (LDO) regulator is incorporated to provide a regulated 4.7 V supply for the circuitry. The 4.7 V supply will enable higher applied voltages and higher actuation currents than 3.3 V supply. The current-source DACs utilized are two Texas Instruments DAC63004, each having N_{dac} = 8-bit resolution with four outputs and can provide variable applied voltage V_i in the range from 0 to V_{CC} = 4.7 V at each of its outputs. Each output can provide a current I_i in the range from 0 to $I_{max} = 50 - 250$ μA. As shown in Figs. 2a and 3, each output is connected to a current sense resistor, R_i = 10 kΩ±0.1%, which in turn is connected to an electrode (Ag, AgCl, or Pt wires) in the PDMS. Each electrode can be set as either the WE (by setting $I_i > 0$ μA) or the RE (by setting V_i = 0 V) for a specified duration. Additionally, each output can also be set to a high-impedance (Hi-Z) state which electronically disconnects the current source from its electrode, resulting in a channel current $I_i \approx 0\,\mu A$ (open circuit). This feature allows disabling of individual channels and provides better spatial control of actuation if/when needed. Moreover, the current-source DACs enables rapid current control with negligible delay across all eight channels.

As shown in Fig. 3, two eight-input ADCs are utilized to measure voltage drop across each resistor R_i. Operational amplifiers (op-amps) configured as voltage buffers are utilized at the ADC inputs to present very high input impedance which prevents current loading due to the ADC and enables accurate measurement of actuation currents. A dedicated pair of inputs of the ADCs is connected across each resistor R_i to measure the voltage drop. The ADC utilized is Burr-Brown ADS7828 and has a N_{adc} = 12-bit resolution which translates to 0.8 mV for voltage and 0.08 μA for current measurements. Both the DAC and ADC support the I^2C fast mode in which the clock speed is set to 400 KHz that allows the MCU to set or measure voltages at < 0.1 ms interval. The I^2C pins of the MCU, SCL and SDA, are pulled up externally by strong pull-up resistors (2 kΩ) to allow fast rise times (to meet setup and hold time requirements) needed for the fast mode. The ADCs sample the analog applied V_i and electrode V_{E_i} voltages across each resistor R_i and convert them into 12-bit integers, for each channel. A burst of sixteen samples is taken at each input, spaced 0.5 ms apart. The MCU then finds the average of these samples to reduce noise. The sampling interval between the averages is 0.1 s. The MCU stores these point-averaged N_{adc} = 12-bit integer codes A_i and

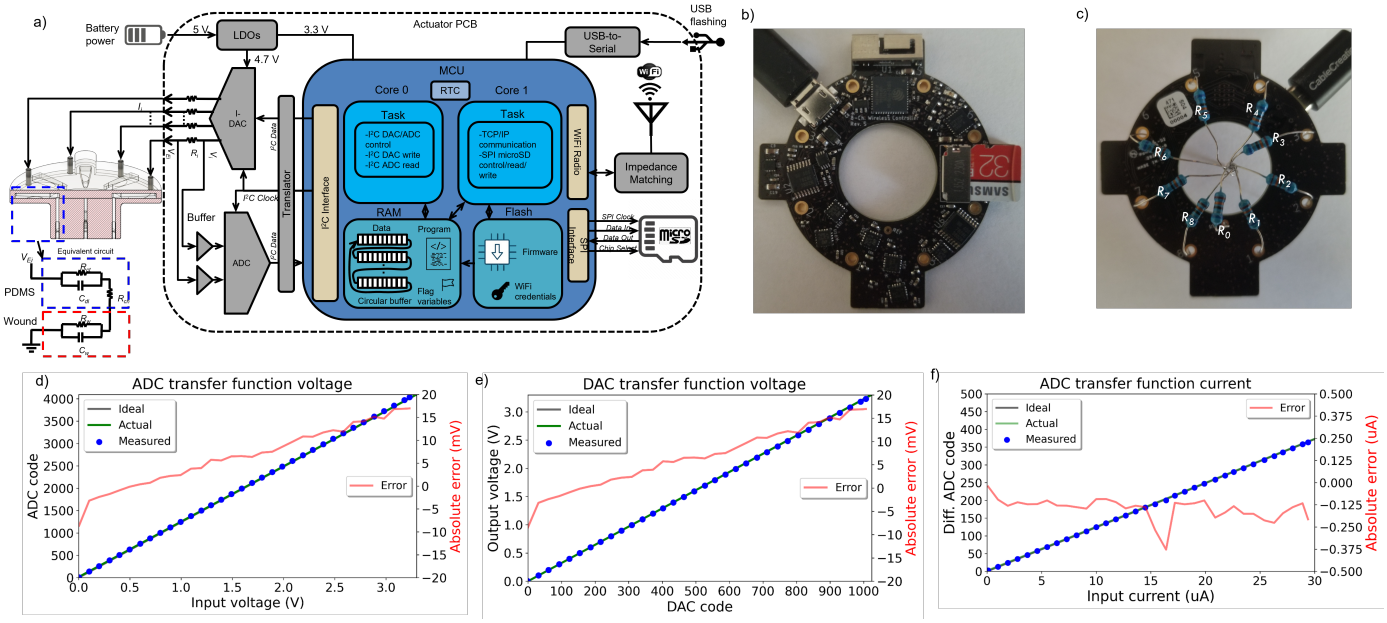

Fig. 2. a) Simplified circuit diagram of the controller. b) Top view of the prototype. c) Bottom view of the prototype with resistors soldered between each channel and center resistor to verify current measurements. d) ADC transfer function for voltage measurements. e) Current-source DAC transfer function. f) ADC transfer function for current measurements.

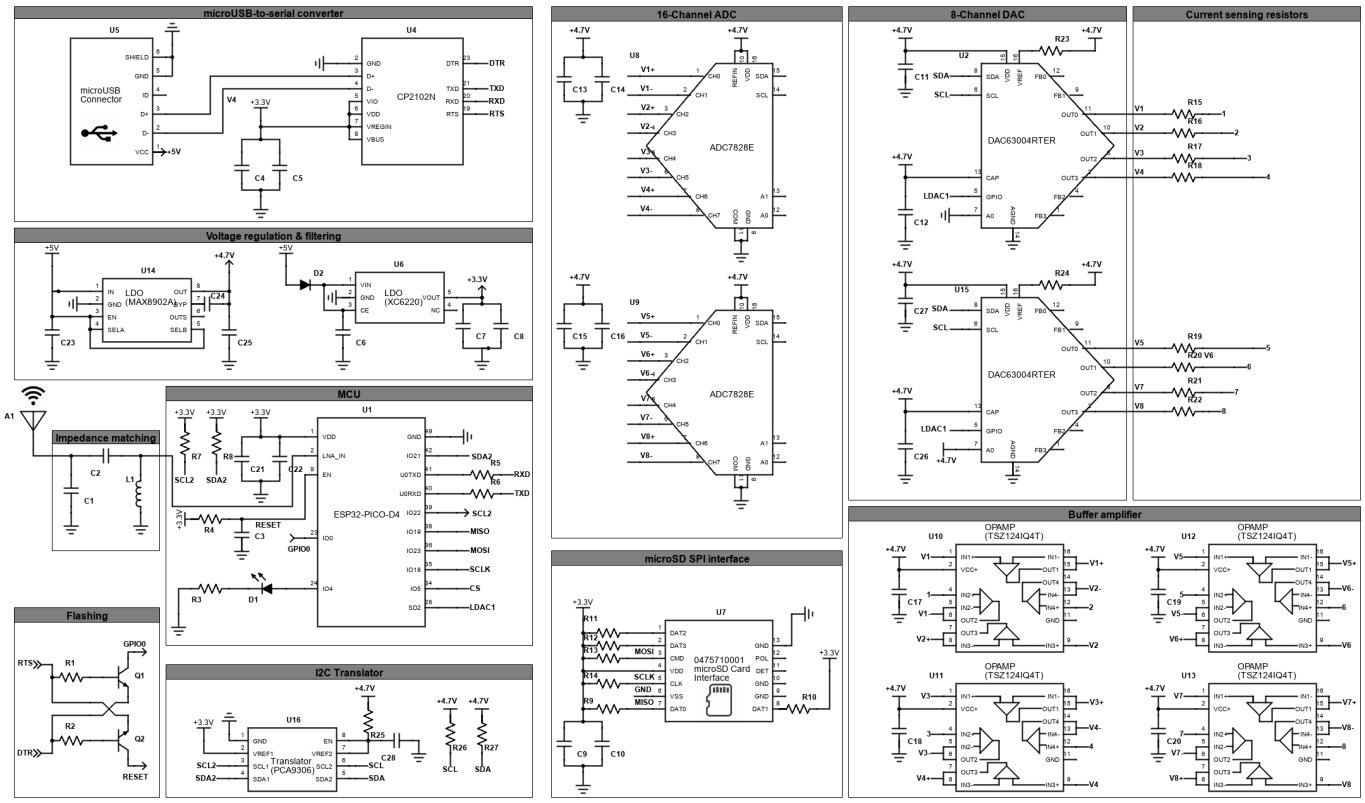

Fig. 3. Detailed circuit diagram of wireless bioelectronic device showing the interconnection between the MCU, ADCs, DACs, opamps, microSD card, USB-to-serial converter, LDOs, power supply, flashing circuit, antenna, impedance matching network, SPI and I^{2}C interfaces.

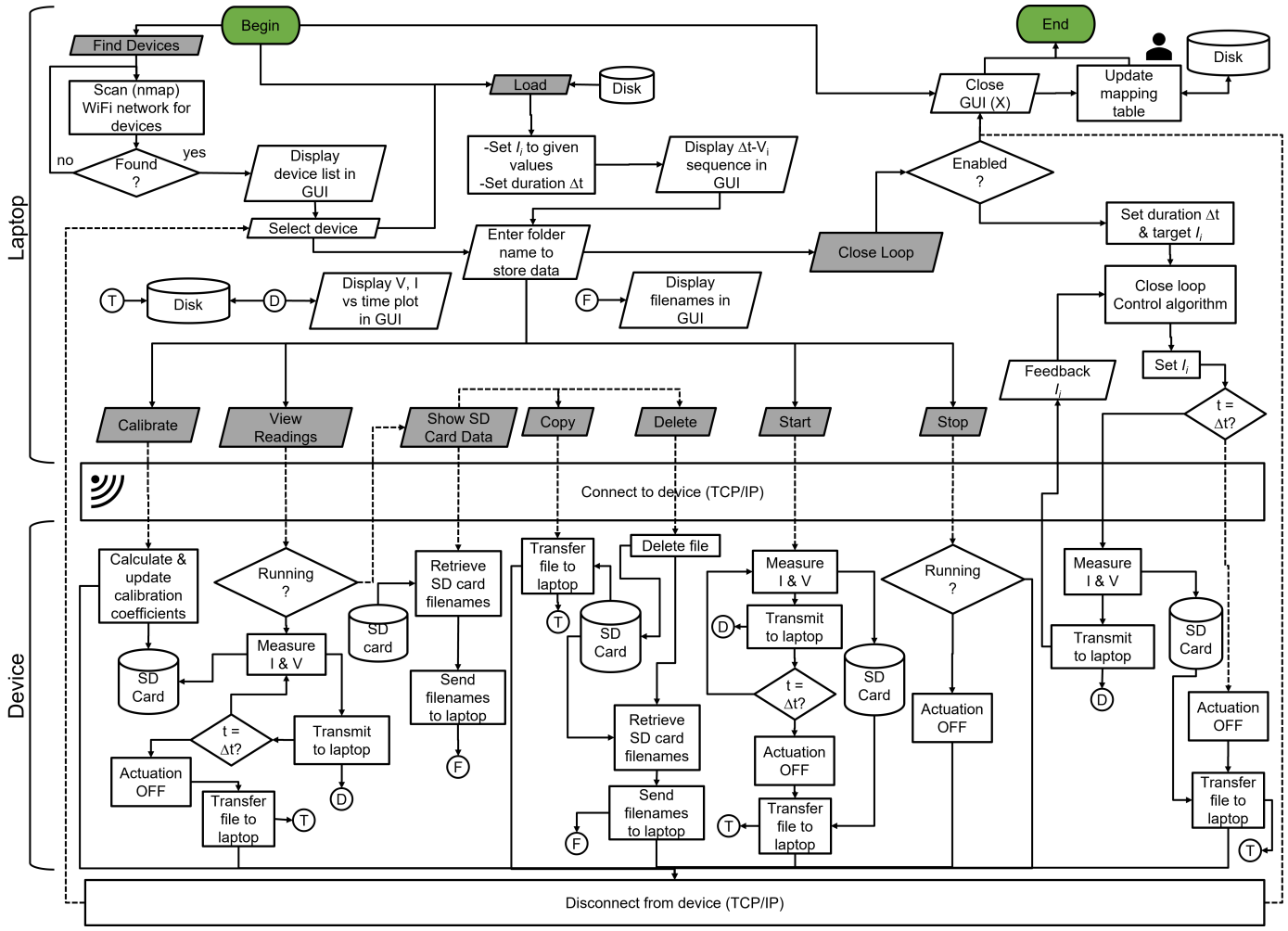

Fig. 4. Flowchart for data acquisition and control showing the communication between a laptop and wireless bioelectronic device. The GUI that is running on a laptop consists of several buttons which are represented by gray parallelograms. Each button press generally establishes a TCP/IP connection to a selected device via the local WiFi network. The device then performs specific tasks such as calibration, data viewing, file viewing, file transfer, file deletion, starting open-loop actuation, stopping actuation, and closed-loop control, depending on the button being pressed.

Parameter	Specifications
Channels	8-actuation (DAC), 16-sensing (ADC)
Applied voltage V_i	0 to 4.7 V
Channel current I_i	0 to 50-250 μA
Actuation resolution	8-bit DAC (0.2-1 μA)
Sensing resolution	12-bit ADC (1.1 mV)
Averaging factor	16
Sampling period	100 ms
Power management	Active/light sleep/standby
Typical delivery duration	24 h per day (up to 7 d)
microSD card size	4 to 32 GBytes
Current sensing resistors R_i	10 kΩ±0.1%

Table 2: Specifications of wireless biolectronic device.

A_{E_i}, for applied voltage and electrode voltage, respectively, on the microSD card via the SPI bus for each channel i. The average applied V_i and electrode V_{E_i} voltages at each channel i can be found as

$$V_{i/E_i} = \frac{A_{i/E_i}}{2^{N_{adc}}} V_{CC} \tag{4}$$

The voltage drop, $(V_i - V_{E_i})$, across resistor R_i can then be used to find current flowing at each channel i as

$$I_i = \frac{V_i - V_{E_i}}{R_i} \tag{5}$$

Eqs. (4) and (5) allow calculation of voltage and current at each channel when the ADC and DAC codes are not calibrated and represent the ideal transfer functions of the device. When both ADC and DAC codes are calibrated using two-point calibration method, the voltage and current at each channel are calculated using Eqs. (S5) and (S12), respectively, which results in more accurate measurements (since the noise is calibrated out) and represent the actual transfer functions of the device.

The ideal and actual voltage transfer functions of the ADCs and DACs for channel 1 are shown in Fig. 2d and e along with absolute error between measured and true voltages, all of which are obtained from Supplementary Eqs. (S1) [ideal ADC], (S4) [ideal DAC], (S5) [actual ADC], and S8 [actual DAC], as the DAC output code D_i is varied from 0 to $2^{N_{dac}} - 1$. True values of voltage at the DAC output voltage/ADC input, in steps of 0.1 V are obtained with a multimeter and the corresponding codes measured by the device are recorded. When the true and measured values are plotted against one other, the measured curve closely follows the ideal/actual transfer function curves indicating that the device has excellent voltage measurement accuracy over the entire voltage range.

The ideal and actual current transfer function of the ADC when a load resistance of R_i = 100 kΩ is used at channel 1 along with with absolute error between measured and true currents, is shown in Fig. 2f, which are obtained from Supplementary Eqs. (S2) and (S11), respectively. True values of the current in steps of 0.1 μA are obtained with a multimeter that is placed in series with the load resistance R_i = 100 kΩ and the corresponding current measured by the device are recorded. The measured curve thus obtained closely follows the ideal/actual current transfer function curves indicating that the device has excellent current measurement accuracy within the 30 μA current range.

The MCU and microSD card are powered from the 3.3 V rail, as they do not support higher supply voltages. For I^2C communication, a 3.3 V to 4.7 V level translator chip is employed to handle the logic level differences between the MCU and ADCs/DACs. The translator mediates the difference in operating voltage levels between the MCU (3.3 V) and ADCs/DACs (4.7 V) of their respective I^2C clock and data signals.

Table 2 lists the main controller specifications. The I^2C communication between MCU (master) and DACs/ADCs (slaves) is achieved as follows. To start communication, the master sends a START condition on the I^2C bus (switching SDA line from HIGH to LOW followed by switching SCL line from HIGH to LOW). The MCU then sends a 7-bit address of the slave it wants to communicate with followed by a read(HIGH)/write(LOW) bit (called the address byte as a whole) on the SDA line. All the slaves read each bit serially. Each bit is read when the SCL is HIGH, and therefore, it takes 8 clock cycles to read a byte. The slave with the matching address acknowledges by pulling the SDA line LOW on the 9th clock cycle. After that, the MCU typically writes a control byte to configure the slave (e.g., select a ADC/DAC channel to read/write, power up/down channels, etc.) which is acknowledged by the slave. Then, one or more data bytes are transferred between the MCU and a slave (e.g., read a voltage measurement from the ADCs, set a voltage at the DAC output). After each byte is transferred, the receiver acknowledges the sender. Finally, to stop communication, the master sends a STOP condition on the I^2C bus (switching SCL line from LOW to HIGH followed by switching SDA line from LOW to HIGH).

3.2.2. *GUI and laptop software*

As illustrated in Fig. 1b, the wireless bioelectronic device can be controlled using a laptop on any local WiFi network which can be set up using a commercial router. To validate that the device is working properly, the real-time current and voltage measurements made by the device are first verified by setting a target current across a known resistor of 1.2 MΩ at all eight outer and center channels, respectively, as shown in

Fig. 2c. The GUI and data acquisition/control software are written in Python using the Spyder (anaconda3) IDE environment. The user flow diagram for the GUI (software) on the laptop, and the subsequent, instruction flow (firmware) on the devices, is shown in Fig. 4. The GUI includes push-buttons for scanning the WiFi network to find all connected devices (Find Devices), drop-down menu to select a device from multiple devices found, loading the actuation table (Load), showing the actuation table, close loop control (Close Loop), calibrating the DAC and ADC (Calibrate), real-time viewing of measured voltages/currents (View Readings), displaying SD card data on the device (Show SD Card Data), transferring file from the device to the laptop (Copy), deleting file on the device (Delete), and starting (Start) or stopping the actuation (Stop). When the device is powered up, it automatically connects to the network and the router assigns a unique IP address to each connected device. The remote laptop is also connected to the same network. When 'Find Devices' button is pressed in the GUI, the network is scanned to find connected devices and each device is uniquely identified using their media access control (MAC) address/IP address. When a user wants to initiate a certain action on the selected device (e.g., by pressing the 'Start' button), the laptop first establishes a TCP/IP connection with the device and sends a unique high-level command to the device indicating the action to be performed, as depicted in Fig. 4. On the device side, these commands are uniquely identified and appropriate sequence of tasks are carried out by the firmware. For example, to start the actuation, at first, the fixed-duration sequence of voltages to be applied is loaded from a .csv file by pressing the 'Load' button and selecting the file on the laptop. Second, the 'Start' button is pressed which instructs the device firmware to apply the specified sequence of voltages, measure the currents, and then, transmit data in real-time to the laptop wirelessly for immediate viewing. Moreover, for redundancy/reliability, the data is also stored locally on the microSD card at a higher sampling rate due to its low latency compared to WiFi. This data is transferred to the remote laptop automatically after the completion of the actuation.

3.2.3. *Device firmware and MCU flashing*

When the high-level commands are received by the device, the firmware breaks them into a sequence of low-level tasks for the MCU to execute, as depicted in Fig. 4. The device firmware is a control program written in C++ using the Arduino IDE environment. Once the device completes the action, it is disconnected from the laptop and put into standby so that it can accept further commands from the laptop. As shown in Fig. 3, the actuator PCB houses a universal serial bus (USB)-to-universal asynchronous receiver and transmitter (UART) bridge called CP2102N (IC from Silicon Labs) that allows us to directly connect the board to a laptop's USB port for flashing the MCU with the firmware and debugging the MCU's firmware. The main tasks the firmware performs are TCP/IP communication, data acquisition (through ADC) and control (through DAC), and reading from/writing to microSD card, distributed between the two cores of the MCU, as depicted in Fig. 2a. The microUSB connector on the PCB is used as an interface for flashing/powering purposes using a USB-A/C cable, connected to a power source. The microUSB connector's D+ and D- data pins are connected to the UART bridge for data transfer, as shown in Fig. 3. The bridge itself is connected to the MCU for transmitting and receiving UART data through the TxD and RxD pins. The process of flashing the PCB takes less than 1 min due to the 3 Mbps transfer rates supported by the UART bridge. The MCU is put into the flashing mode by the UART bridge through the use of RTS and DTR pins which are connected to two transistors that control the state of the MCU pins, IO0 and EN, as shown in Fig. 3. By putting the IO0 and EN pins through a set sequence of logic HIGH and LOW states, the UART instructs the MCU to initiate the flashing mode for downloading firmware. The firmware is then transferred to the flash memory of the MCU via the RXD pin. All of these low level operations are handled internally by the Arduino IDE during the flashing process. Print statements are used in the firmware to send device status updates to the UART bridge via the TxD pin and then sent to the laptop through the USB for display/debugging on Arduino IDE's serial monitor. The firmware can be simply updated by re-flashing the MCU's memory.

3.2.4. *microSD card interface*

SPI communication protocol is used for data transmission between the MCU (master) and the microSD card (slave), as illustrated in Fig. 3. Four default SPI pins of the MCU: MOSI (23), MISO (19), SCLK (18), and CS (5) are connected to the CMD, DAT0, CLK, and DAT3 pins, respectively, of the microSD card connector to provide full-duplex communication. SPI mode 0 is used for data transfer. This means that the SCLK (clock) signal stays LOW when there is no data transmission (i.e., CS is HIGH) and data is simultaneously received (on the MISO pin) on rising edge and transmitted (on the MOSI pin) on the falling edge of the clock by the MCU. As indicated in Fig. 3, the SPI pins are pulled-up by 10 kΩ resistors to provide faster rise times needed for high-speed microSD cards than would otherwise be achieved by weak internal pull-up resistors (45 kΩ) of the MCU. Pull-up resistors of 10 kΩ are also used on the SD card pins DAT0 - DAT3 even though they are not connected to the MCU (since SPI mode is being used) to prevent the card from entering a wrong state.

3.2.5. *Antenna and impedance matching*

As shown in Figs. 1a, a 3D metal antenna is used for transmitting and receiving 2.4 GHz radio signals for WiFi communication. The antenna is tuned to this frequency using a π-matching network which is connected to the LNA pin of the MCU, as illustrated in Fig. 3. The matching network maximizes power transfer between the LNA and antenna at 2.4 GHz. The PCB board material, thickness, trace width/length, and proximity of other electronic components dictate the value of capacitors C_1, C_2, and inductor L required for adjusting the resonant frequency of the antenna. Based on manufacturer's recommendation, the following values were utilized: C_1 = 2.7 pF, C_2 = 4.7 pF and L = 1.6 nH. These values are essentially used to cancel out the parasitic reactance (capacitance and inductance) associated with transmission lines that are routed from

the LNA to the antenna input. The antenna is surface mounted at the edge of the board to minimize the shift in the resonant frequency and interference due to nearby circuits/components. The PCB comprising the matching network and the antenna was simulated in COMSOL using finite element method. The reflection coefficient S_{11} at the matching network input was found to be -15.3 dB at 2.45 GHz, which indicates that 97% of the power provided by the LNA is accepted by the antenna. The maximum gain of the antenna is 1.2 dBi. Fig. 1a shows the 3D gain pattern of the antenna and how it aligns with the antenna itself.

3.2.6. Closed-loop control of current

Fig. 5 shows a simple high-level diagram of how the wireless bioelectronic device operates during close loop control of current. The close loop begins by gradually stepping up the target current. To maintain target levels, the onboard current-source DACs rapidly adjust (increases or decreases) the applied voltage at each channel without noticeable delays. The currents can change due to the dynamic nature of the contact and wound resistance as well as the animal itself. Therefore, current sources provide the fastest feedback and adjust the applied voltage rapidly. The currents are pulsed at a 92.3% duty cycle (HIGH for 60 s, LOW for 5 s) to allow electrodes to charge and discharge.

3.2.7. Power consumption

The devices take advantage of sleep mode to reduce overall power consumption when they are not actuating, during long in vivo experiments. Table 3 shows the different operating modes of the device and typical current consumed by the board in each mode. Since each device can generally reach the target dose within 6 hours of actuation, the device can be put into sleep mode for the rest of the day to save power. During the experiment, the power banks connected to the devices can only be replaced once a day due to handling limitations. The use of sleep mode provides enough power saving to allow multiple devices to run and actuate on their respective wounds each day.

3.3. Experimental results

7-day Flx delivery was carried out on pig wounds. For Flx delivery, the current level dictates the delivery rate which combined with the actuation duration dictates the total delivered dose. The actuation duration in the in vivo experiment was set to 23 h to reach a target dose of approximately 0.25 mg of fluoxetine delivered per day per wound. For EF delivery, the current level dictates the strength of applied EF.

Closed-loop control of current is performed to achieve and maintain specific target levels (i.e., delivery rate) using onboard current source DACs directed by the wound healing algorithm running on the remote laptop, as illustrated in Fig. 1b. The target currents are varied to verify the ability of the algorithm to set and track changing targets. The actuation duration is set to 23 hours per day. On Day 0, Flx is not delivered and Flx is delivered as dictated by the algorithm. From Day 1 onwards, the algorithm switches to Flx delivery from even channels (2, 4, 6, 8) at the 6-hour mark.

In each actuated wound, the applied voltages at all 8 outer channels are adjusted continously by the current-source DACs to achieve the target levels. The measured currents and voltages on Day 6 at one of the Flx-treated wounds are shown in Fig. 6a. The dose delivered on each day is shown in Fig. 6b.

The device firmware has been optimized to reduce communication latency by efficiently multitasking between data acquisition/control and handling TCP/IP commands from the laptop. This also significantly reduced data acquisition gaps and control action delay, enabling the device to capture/control fast changing currents.

The firmware takes advantage of multicore processing. The MCU on the device has two cores: 0 and 1, as depicted in Fig. 2a. Core 0 is dedicated for sampling data from the ADCs and changing the DAC output voltage while core 1 is dedicated to handling TCP/IP commands for WiFi communication with the remote laptop and reading/writing to microSD card. During actuation, the data from the ADC comes at a faster rate than that can be wireless transmitted. Core 0 stores the measured ADC data into a sequence of allocated memory buffers while Core 1 sends the data in a FIFO fashion to the laptop while also recording it on a microSD card. This allows the system to record the data at higher sampling rates than would otherwise be possible. The number of buffers and buffer size must be high enough to prevent overfill and data loss and it is determined by the worst-case latency of WiFi transmission which is around few seconds. As illustrated in Fig. 2a, the buffers are referenced in a circular fashion for efficient utilization of memory. Intercore communication is handled through flag variables in the integrated 4-MB SPI flash of the MCU. The data is continuously sampled, only pausing momentarily (< 1 s) to avoid race conditions, when a new close loop command is received and applied voltages must be changed.

Furthermore, software and firmware improvements are made on the laptop and device to handle occasional communication and power loss scenarios. When communication failures occur, network exceptions are raised which are handled on the laptop by continuously attempting to reestablish connection with the device. Moreover, a resume feature is incorporated in the firmware which checks the last recorded timestamp on the microSD card at every device boot up. In the event of a power failure, this timestamp can be used to determine whether the last actuation was completed. If the actuation duration is less than 6 h, default actuation is first activated, and shortly after, the laptop can reestablish connection with the device to resume close loop control.

3.4. Fluoxetine dose calculation

For Flx delivery, the reservoirs are filled with 10 mM Flx HCl solution, and the capillaries are loaded with Flx^+ cations. The currents measured by the wireless bioelectronic device are directly proportional to the rate of Flx delivery. To quantify the overall treatment dose, the currents at each channel can be cumulatively integrated and added to calculate the dose delivery for Flx treatment. The accumulated charge exchange Q_i at

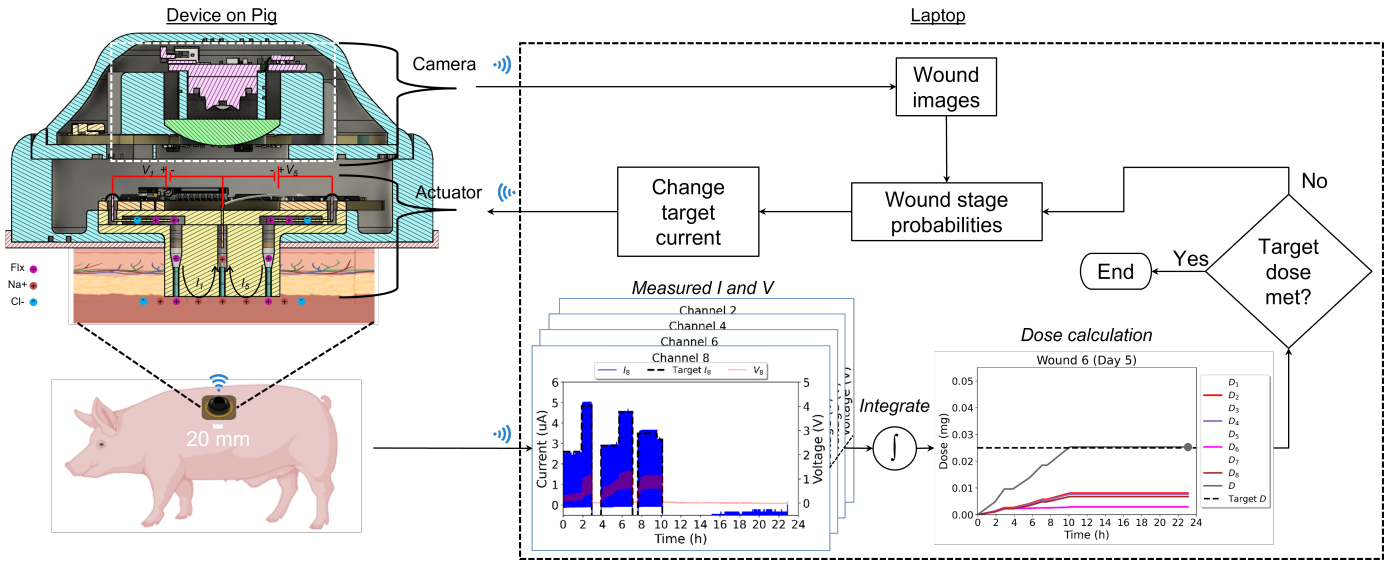

Fig. 5. Closed-loop control of current on the wireless bioelectronic device using onboard current source DACs with pulsing. The target currents are determined by the wound healing algorithm based on wound stage probabilities.

Operating mode	Current (mA)	Comments
Sleep	25	No actuation, WiFi disabled, can be woken up after a preprogrammed time to put into standby mode
Standby	50	No actuation, WiFi connected, ready to accept commands
Actuation (No transmission)	70	Data recorded on SD card, no transmission to laptop
Actuation (Transmission)	100-180	Data recorded on SD card and real-time transmission to laptop via WiFi

Table 3: Current drawn by the wireless bioelectronic device in different operating modes.

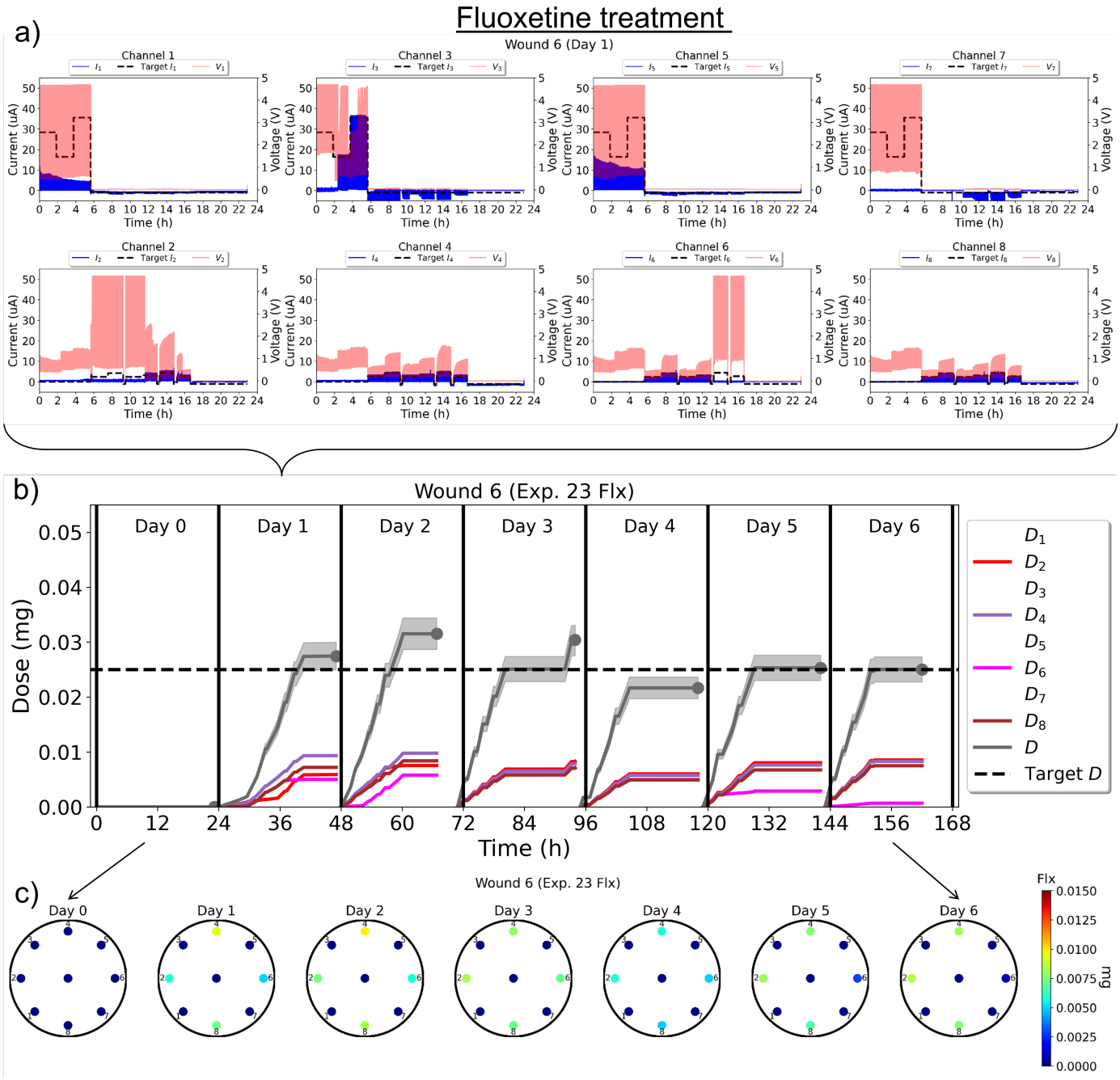

Fig. 6. Experimental data of 7-day Flx$^+$ delivery on a wound. a) Measured applied voltages and currents at the 8 channels on Day 1. b) Temporal variation of accumulated channel and total dose during 23-hour delivery window on each day. c) Spatial variation of accumulated channel and total dose delivered at the end of the 23-hour delivery window on each day.

channel i at time t can be calculated as,

$$Q_i(t) = \int_{t_{start}}^{t} I_i(\tau)d\tau \qquad (C) \tag{6}$$

The total accumulated charge exchange Q (in Coulomb) is the sum of charge exchanges at all channels i = 1 to 8 and is given by,

$$Q(t) = \sum_{i=1}^{8} Q_i(t) \qquad (C) \tag{7}$$

For Flx treatment, the accumulated dose D_i at channel i at time t can be calculated by integrating only the positive currents $I_i^+(t) = I_i(t) \geq 0$ as follows:

$$D_i(t) = \frac{\eta Q_i^+(t)}{F} M \qquad (g) \tag{8}$$

where $\eta = 2.2 \pm 1.1\%$ is the average Flx^+ delivery efficiency of the device (Li et al., 2023a), M = 309.33 g/mol is the molar mass of Flx, F = 96485.3321 C/mol is the Faraday's constant, and $Q_i(t) = \int_{t_{start}}^{t} I_i(\tau)d\tau$.

The reason why only contributions of positive currents are integrated is because Flx delivery is assumed to happen only when the current is positive (i.e., Flx^+ cations flow from the reservoirs, through the cation-selective hydrogel, and to the wound bed) and diffuses away in the blood stream. When current is negative, endogenous cations such as Na^+ carry the current to the reservoirs to maintain charge balance and do not negate the Flx delivery. Hence, the positive and negative currents are due to the exchange of different types of ions, i.e., Flx^+ and endogenous cations, respectively.

The total accumulated dose D (in grams) can be calculated by summing the accumulated channel dose D_i at all channels i = 1 to 8, as follows:

$$D(t) = \sum_{i=1}^{8} D_i(t) \qquad (g) \tag{9}$$

Using Eqs. 8 and 9, the temporal variation of accumulated channel dose D_i and total dose D from measured currents (given in Fig. 6a) was calculated for Day 6, as shown in Fig. 6b. The spatial variation showing the channel dose D_i at the wound edges and center at the end of Day 6 is shown in Fig. 6c. The dose delivery is not uniform across the wound. This is attributed to the variation in the current at each channel caused by differences in contact and channel resistance. If the resistance is too high (e.g., due to poor contact or capillary), the maximum voltage (i.e., V_{CC} = 3.3 V supply) that can be applied will not be able to attain target current at the channel.

Furthermore, Fig. 6b and c shows the entire spatiotemporal progression of fluoxetine delivery at the wound over a period of 7 days. The dose delivery associated with the bioelectronic device is gradual which helps to improve bio-availability, as opposed to oral or topical drug delivery. The start of actuation is represented by a vertical line. The actuation typically begins anywhere from 12:00 PM to 2:00 PM and continues for 23 h. The total accumulated dose D (represented by a gray dot) on each day varies a little bit even though the target dose is the same.

The slope of D_i indicates the delivery rate at that channel and can be used to gauge how each channel is functioning. The higher the slope, the higher the delivery rate. A slope of zero (i.e., flat D_i) indicates that the delivery rate is zero at that point in time. For example, on Day 2 after the 60-hour mark, D_2, D_4, D_6, and D_8 have near zero slopes indicating near-zero or negative currents and the associated channels are not delivering Flx, as shown in Fig. 6b. Meanwhile, before the 60-hour mark, D_2, D_4, D_6, and D_8 have positive slopes indicating positive currents and the associated channels are delivering Flx. The center channel has negative currents (not shown) since it is the return path for the channel currents I_i and does not deliver any Flx, as indicated by the blue dot at the center in Fig. 6c. From the temporal and spatial dose profile of each channel in Fig. 6b and c, it is easy to see Days 1-3 have more and better functioning channels than other days.

3.5. M1/M2 ratio

Quadruple staining of the pig tissues is done to reveal the count of M1 and M2 macrophages and find the M1/M2 ratio for Flx-treated wound. The antibodies were determined and the staining protocols were used, as indicated in the *Methods: Macrophage IHC staining* section to label M1 and M2 marker cells with iNOS and Arginase I, respectively, in the background staining of pan-macrophage M0 marker CD68, as shown in Fig. 7a for a Flx-treated wound.

Imaging of the whole wound allows the determination of spatial distribution of M1 and M2 markers throughout the wound, as shown in Supplementary Fig. S1.

In the healing wound without treatment (i.e., control wound), wound edges appear to have a lower M1/M2 ratio indicating the advancing of the wound edge earlier into the proliferation/regenerative phase than the wound center. Furthermore, there is a tendency for the M1/M2 ratio to decrease over time as the wound healing process advances (comparing Day 3 to Day 7). Flx treatment significantly reduced M1/M2 ratio by 70.2%, indicating enhanced proliferation status, which is more obvious at the wound edge, but has no effect at the wound center. The ratio at the wound edge after 3 days of treatment significantly decreases to level similar to the control group at around 7 days. From the total number of M1 and M2 cells, the reduction of M1/M2 ratio at the wound edge appears to be mainly due to the reduction of M1 marker-positive cells. This suggests that fluoxetine treatment selectively affects M1 macrophages at the wound edge at early stages of wound healing, leading to a shift in the M1/M2 balance toward a less inflammatory state.

3.6. Re-epithelialization

To determine re-epithelialization, one half of the wound tissue excised and bisected from a pig, was fixed in 4% paraformaldehyde, and then processed and embedded in paraffin for sectioning. 5 μm sections were generated and stained with the H&E staining protocol, as described previously in the *Methods: Histology* section. Representative Flx-treated and

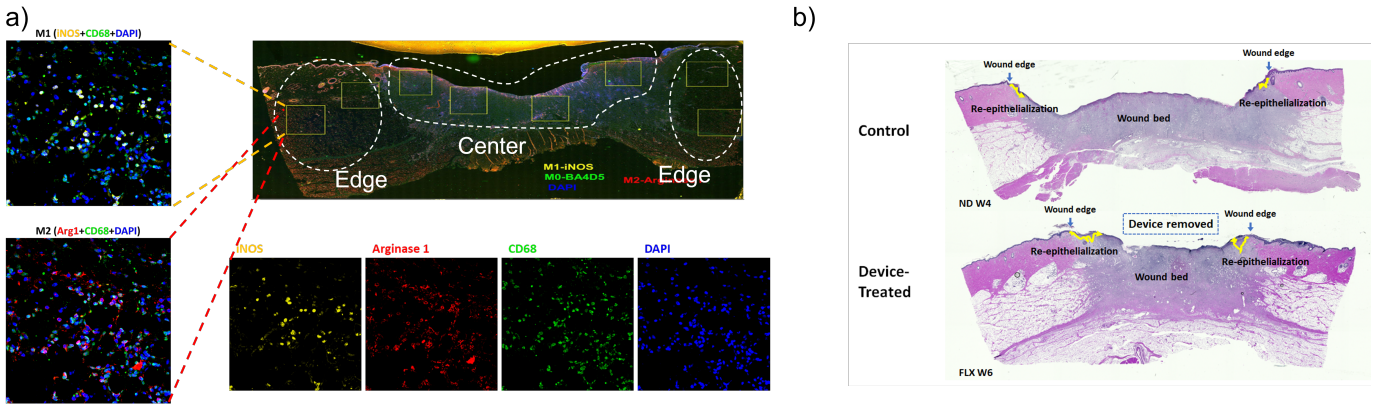

Fig. 7. a) Confocal images of co-staining of M0, M1, and/or M2 markers in a Flx$^+$-treated wound on Day 3 showing the sampled center and edge regions. DAPI is added as a counterstain. The merged images are in the upper panel, with the four-color separation images in the lower panel. b) Representative images showing re-epithelialization on Day 7 for control (top) and Flx$^+$-treated (bottom) wound tissues. Wound edge in each image is indicated by blue arrows, and the re-epithelialization is highlighted by yellow arrows extended from the wound edge to the right. Scale bar = 2 mm.

control wound images from an Flx delivery experiment are shown in Fig. 7b. The re-epithelialization which indicates the size of the newly formed epithelium is indicated by the yellow arrows. The images were scored to determine the percentage of wound closure (referred to here as % re-epithelialization). Beginning at the innermost edge of the mature collagen (wound edge, blue arrows), we measured the length of the epithelial tongues and the width of the entire wound (yellow arrows). From these distances, we calculated the percentage of closure for each wound. The Flx treatment increased re-epithelialization by 39.5% on Day 7 when compared with control device without Flx treatment.

4. Conclusions and Future work

In this study, we demonstrate the design, development, and verification of our wireless bioelectronic system for wound healing in vivo. The devices are used to deliver fluoxetine and electric field treatments, separately, in full-thickness wounds in pig models. Each treatment is applied continuously for 23 h per day for a period of 7 days. IHC staining results show that a Flx-treated wound had improved M1/M2 ratio compared to a control wound by 70.2% at the wound center. Meanwhile, H&E staining results show that a Flx-treated wound had improved re-epithelialization compared to a control wound by 39.5%. More animal experiments are currently being conducted to see if statistical significant can be achieved. We are also conducting experiments to better understand and correlate the actuation parameters and biological response in order to find the optimal timing and dose of the Flx and EF treatments for accelerating wound healing.

CRediT authorship contribution statement

Prabhat Baniya: Conceptualization, PCB design, PCB-PDMS integration, Methodology, Hardware, Software, Validation, Formal analysis, Writing - original draft, Visualization, Investigation. Maryam Tebyani, Kaelan Schorger: PDMS design, PDMS fabrication, Investigation. Wan Shen Hee: Camera design and integration, Investigation. Houpu Li, Narges Asefifeyzabadi, Cristian Hernandez: Performed ion-pump experiments, Investigation. Celeste Franco: 3D printing of enclosures. Alexie Barbee: PCB-PDMS integration. Hsin-ya Yang: Performed animal experiments. Kan Zhu, Cynthia Recendez: M1/M2 macrophage quantification, Investigation. Fan Lu: Close loop. Anthony Gallegos: Re-epithelialization, Investigation. Marco Rolandi: Supervision, Funding acquisition, Project administration, Resources. Mircea Teodorescu: Supervision, Funding acquisition, Project administration, Resources.

Declaration of competing interest

The authors declare that they have no known competing financial interests or personal relationships that could have appeared to influence the work reported in this paper.

Acknowledgements

This research is supported by the Defense Advanced Research Projects Agency (DARPA) through Cooperative Agreement Number D20AC00003 awarded by the U.S. Department of the Interior (DOI), Interior Business Center.

Appendix A. Supplementary data

Supplementary information to this article is attached at the end.

References

Asefifeyzabadi, N., Nguyen, T., Li, H., Zhu, K., Yang, H.y., Baniya, P., Medina Lopez, A., Gallegos, A., Hsieh, H.C., Dechiraju, H., Hernandez, C., Schorger, K., Recendez, C., Tebyani, M., Selberg, J., Luo, L., Muzzy, E., Hsieh, C., Barbee, A., Orozco, J., Alhamo, M.A., Levin, M., Aslankoohi, E., Gomez, M., Zhao, M., Teodorescu, M., Isseroff, R.R., Rolandi, M., 2024. A pro-reparative bioelectronic device for controlled delivery of

ions and biomolecules. Wound Repair and Regeneration 32, 709–719. doi:https://doi.org/10.1111/wrr.13191.

Bakshi, P., Vora, D., Hemmady, K., Banga, A., 2020. Iontophoretic skin delivery systems: Success and failures. International Journal of Pharmaceutics 586, 119584. doi:https://doi.org/10.1016/j.ijpharm.2020.119584.

Baniya, P., Tebyani, M., Asefifeyzabadi, N., Nguyen, T., Hernandez, C., Zhu, K., Li, H., Selberg, J., Hsieh, H.C., Pansodtee, P., et al., 2023. A system for bioelectronic delivery of treatment directed toward wound healing. Scientific Reports 13, 14766.

Cascales, J.P., Roussakis, E., Witthauer, L., Goss, A., Li, X., Chen, Y., Marks, H.L., Evans, C.L., 2020. Wearable device for remote monitoring of transcutaneous tissue oxygenation. Biomed. Opt. Express 11, 6989–7002. doi:10.1364/BOE.408850.

Chen, Y., Liang, Y., Liu, J., Yang, J., Jia, N., Zhu, C., Zhang, J., 2021. Optimizing microenvironment by integrating negative pressure and exogenous electric fields via a flexible porous conductive dressing to accelerate wound healing. Biomaterials science 9, 238–251.

Chi, J., Zhang, X., Chen, C., Shao, C., Zhao, Y., Wang, Y., 2020. Antibacterial and angiogenic chitosan microneedle array patch for promoting wound healing. Bioactive Materials 5, 253–259. doi:https://doi.org/10.1016/j.bioactmat.2020.02.004.

Dechiraju, H., Selberg, J., Jia, M., Pansodtee, P., Li, H., Hsieh, H.C., Hernandez, C., Asefifeyzabadi, N., Nguyen, T., Baniya, P., Marquez, G., Rasmussen-Ivey, C., Bradley, C., Teodorescu, M., Gomez, M., Levin, M., Rolandi, M., 2022. On-chip on-demand delivery of k+ for in vitro bioelectronics. AIP Advances 12, 125205. doi:10.1063/5.0129134.

Del Bono, F., Bontempi, A., Dentis, A., Di Trani, N., Demarchi, D., Grattoni, A., Ros, P.M., 2023. Design of a closed-loop wireless power transfer system for an implantable drug delivery device. IEEE Sensors Journal , 1–1doi:10.1109/JSEN.2023.3270521.

Derakhshandeh, H., Aghabaglou, F., McCarthy, A., Mostafavi, A., Wiseman, C., Bonick, Z., Ghanavati, I., Harris, S., Kreikemeier-Bower, C., Moosavi Basri, S.M., Rosenbohm, J., Yang, R., Mostafalu, P., Orgill, D., Tamayol, A., 2020. A wirelessly controlled smart bandage with 3d-printed miniaturized needle arrays. Advanced Functional Materials 30, 1905544. doi:https://doi.org/10.1002/adfm.201905544.

Du, S., Zhou, N., Gao, Y., Xie, G., Du, H., Jiang, H., Zhang, L., Tao, J., Zhu, J., 2020. Bioinspired hybrid patches with self-adhesive hydrogel and piezoelectric nanogenerator for promoting skin wound healing. Nano Research 13, 2525–2533.

Freedman, B.R., Hwang, C., Talbot, S., Hibler, B., Matoori, S., Mooney, D.J., 2023. Breakthrough treatments for accelerated wound healing. Science Advances 9, eade7007. doi:10.1126/sciadv.ade7007.

Ghanim, R., Kaushik, A., Park, J., Abramson, A., 2023. Communication protocols integrating wearables, ingestibles, and implantables for closed-loop therapies. Device 1, 100092. doi:https://doi.org/10.1016/j.device.2023.100092.

Jiang, Y., Trotsyuk, A.A., Niu, S., Henn, D., Chen, K., Shih, C.C., Larson, M.R., Mermin-Bunnell, A.M., Mittal, S., Lai, J.C., Saberi, A., Beard, E., Jing, S., Zhong, D., Steele, S.R., Sun, K., Jain, T., Zhao, E., Neimeth, C.R., Viana, W.G., Tang, J., Sivaraj, D., Padmanabhan, J., Rodrigues, M., Perrault, D.P., Chattopadhyay, A., Maan, Z.N., Leeolou, M.C., Bonham, C.A., Kwon, S.H., Kussie, H.C., Fischer, K.S., Gurusankar, G., Liang, K., Zhang, K., Nag, R., Snyder, M.P., Januszyk, M., Gurtner, G.C., Bao, Z., 2022. Wireless closed-loop smart bandage for chronic wound management and accelerated tissue regeneration. bioRxiv doi:10.1101/2022.01.16.476432.

Kar, A., Ahamad, N., Dewani, M., Awasthi, L., Patil, R., Banerjee, R., 2022. Wearable and implantable devices for drug delivery: Applications and challenges. Biomaterials 283, 121435. doi:https://doi.org/10.1016/j.biomaterials.2022.121435.

Khan, A.N., Cha, Y.O., Giddens, H., Hao, Y., 2022. Recent advances in organ specific wireless bioelectronic devices: Perspective on biotelemetry and power transfer using antenna systems. Engineering 11, 27–41. doi:https://doi.org/10.1016/j.eng.2021.10.019.

Li, H., Yang, H.y., Asefifeyzabadi, N., Baniya, P., Lopez, A.M., Gallegos, A., Zhu, K., Nguyen, T., Hernandez, C., Zlobina, K., Recendez, C., Hsieh, H.C., Tebyani, M., Carrión, H., Selberg, J., Luo, L., Alhamo, M.A., Barbee, A., Orozco, J., Hsieh, C., Soulika, A.M., Levin, M., Norouzi, N., Gomez, M., Zhao, M., Teodorescu, M., Isseroff, R.R., Rolandi, M., 2023a. Programmable delivery of fluoxetine via wearable bioelectronics for wound healing in vivo. Advanced Materials Technologies , 2301115doi:https://doi.org/10.1002/admt.202301115.

Li, J., Li, Z., Xiao, J., Nie, C., 2023b. Conformable electrochemical devices for closed-loop wound management. Frontiers in Bioengineering and Biotechnology 11. doi:10.3389/fbioe.2023.1331567.

Liang, Y., Tian, H., Liu, J., Lv, Y., Wang, Y., Zhang, J., Huang, Y., 2020. Application of stable continuous external electric field promotes wound healing in pig wound model. Bioelectrochemistry 135, 107578. doi:https://doi.org/10.1016/j.bioelechem.2020.107578.

Liu, G., Lu, Y., Zhang, F., Liu, Q., 2022. Electronically powered drug delivery devices: considerations and challenges. Expert Opinion on Drug Delivery 19, 1636–1649. doi:10.1080/17425247.2022.2141709. pMID: 36305080.

Liu, J., Liu, Z., Li, X., Zhu, L., Xu, G., Chen, Z., Cheng, C., Lu, Y., Liu, Q., 2020. Wireless, battery-free and wearable device for electrically controlled drug delivery: sodium salicylate released from bilayer polypyrrole by near-field communication on smartphone. Biomedical Microdevices 22, 1–10.

Liu, S., Jia, Z., Yang, F., Ning, T., Gu, X., Niu, X., Fan, Y., 2023. Flexible transient bioelectronic system enables multifunctional active-controlled drug delivery. Advanced Functional Materials 33, 2215034. doi:https://doi.org/10.1002/adfm.202215034.

Long, Y., Wei, H., Li, J., Yao, G., Yu, B., Ni, D., Gibson, A.L., Lan, X., Jiang, Y., Cai, W., Wang, X., 2018. Effective wound healing enabled by discrete alternative electric fields from wearable nanogenerators. ACS Nano 12, 12533–12540. doi:10.1021/acsnano.8b07038. pMID: 30488695.

Mirani, B., Pagan, E., Currie, B., Siddiqui, M.A., Hosseinzadeh, R., Mostafalu, P., Zhang, Y.S., Ghahary, A., Akbari, M., 2017. An advanced multifunctional hydrogel-based dressing for wound monitoring and drug delivery. Advanced Healthcare Materials 6, 1700718. doi:https://doi.org/10.1002/adhm.201700718.

Mori, K., Yamazaki, K., Takei, C., Oshizaka, T., Takeuchi, I., Miyaji, K., Todo, H., Itakura, S., Sugibayashi, K., 2023. Remote-controllable dosage management through a wearable iontophoretic patch utilizing a cell phone. Journal of Controlled Release 355, 1–6. doi:https://doi.org/10.1016/j.jconrel.2023.01.046.

Mostafalu, P., Kiaee, G., Giatsidis, G., Khalilpour, A., Nabavinia, M., Dokmeci, M.R., Sonkusale, S., Orgill, D.P., Tamayol, A., Khademhosseini, A., 2017. A textile dressing for temporal and dosage controlled drug delivery. Advanced Functional Materials 27, 1702399. doi:https://doi.org/10.1002/adfm.201702399.

Mostafalu, P., Tamayol, A., Rahimi, R., Ochoa, M., Khalilpour, A., Kiaee, G., Yazdi, I.K., Bagherifard, S., Dokmeci, M.R., Ziaie, B., Sonkusale, S.R., Khademhosseini, A., 2018. Smart bandage for monitoring and treatment of chronic wounds. Small 14, 1703509. doi:https://doi.org/10.1002/smll.201703509.

Ouyang, Q., Feng, X., Kuang, S., Panwar, N., Song, P., Yang, C., Yang, G., Hemu, X., Zhang, G., Yoon, H.S., Tam, J.P., Liedberg, B., Zhu, G., Yong, K.T., Wang, Z.L., 2019. Self-powered, on-demand transdermal drug delivery system driven by triboelectric nanogenerator. Nano Energy 62, 610–619. doi:https://doi.org/10.1016/j.nanoen.2019.05.056.

Pansodtee, P., Selberg, J., Jia, M., Jafari, M., Dechiraju, H., Thomsen, T., Gomez, M., Rolandi, M., Teodorescu, M., 2021. The multi-channel potentiostat: Development and evaluation of a scalable mini-potentiostat array for investigating electrochemical reaction mechanisms. PLOS ONE 16, 1–14. doi:10.1371/journal.pone.0257167.

Sani, E.S., Xu, C., Wang, C., Song, Y., Min, J., Tu, J., Solomon, S.A., Li, J., Banks, J.L., Armstrong, D.G., Gao, W., 2023. A stretchable wireless wearable bioelectronic system for multiplexed monitoring and combination treatment of infected chronic wounds. Science Advances 9, eadf7388. doi:10.1126/sciadv.adf7388.

Song, K., Ha, U., Lee, J., Bong, K., Yoo, H.J., 2014. An 87-mA · min iontophoresis controller ic with dual-mode impedance sensor for patch-type transdermal drug delivery system. IEEE Journal of Solid-State Circuits 49, 167–178. doi:10.1109/JSSC.2013.2282090.

Vadlapatla, R., Wong, E.Y., Gayakwad, S.G., 2017. Electronic drug delivery systems: An overview. Journal of Drug Delivery Science and Technology 41, 359–366. doi:https://doi.org/10.1016/j.jddst.2017.08.008.

Wentz, C.T., Bernstein, J.G., Monahan, P., Guerra, A., Rodriguez, A., Boyden, E.S., 2011. A wirelessly powered and controlled device for optical neural control of freely-behaving animals. Journal of Neural Engineering 8, 046021. doi:10.1088/1741-2560/8/4/046021.

Xu, G., Lu, Y., Cheng, C., Li, X., Xu, J., Liu, Z., Liu, J., Liu, G., Shi, Z., Chen, Z., Zhang, F., Jia, Y., Xu, D., Yuan, W., Cui, Z., Low, S.S., Liu, Q., 2021. Battery-free and wireless smart wound dressing for wound infection monitoring and electrically controlled on-demand drug delivery. Advanced Functional Materials 31, 2100852. doi:https://doi.org/10.1002/adfm.202100852.